Journal of Energy Chemistry 41 (2020) 60–72

Contents lists available at ScienceDirect

Journal of Energy Chemistry

journal homepage: www.elsevier.com/locate/jechem

http://www.journals.elsevier.com/journal-of-energy-chemistry/

Solar chemical looping reforming of methane combined with isothermal H_2O/CO_2 splitting using ceria oxygen carrier for syngas production

Srirat Chuayboon[a,b], Stéphane Abanades[a,*], Sylvain Rodat[c,d]

[a] Processes, Materials and Solar Energy Laboratory, PROMES-CNRS, Font-Romeu 66120, France
[b] Department of Mechanical Engineering, King Mongkut's Institute of Technology Ladkrabang, Prince of Chumphon Campus, Chumphon 86160, Thailand
[c] Université Grenoble Alpes, Le-Bourget-du-Lac F-73375, France
[d] CEA-LITEN Laboratoire des Systèmes Solaires Haute Température (LSHT), Grenoble F-38054, France

ARTICLE INFO

Article history:
Received 1 February 2019
Revised 25 April 2019
Accepted 6 May 2019
Available online 8 May 2019

Keywords:
Chemical looping
Methane reforming
Ceria structure
Concentrated solar power
Syngas production
H_2O/CO_2 splitting

ABSTRACT

The chemical looping reforming of methane through the nonstoichiometric ceria redox cycle ($CeO_2/CeO_{2-\delta}$) has been experimentally investigated in a directly irradiated solar reactor to convert both solar energy and methane to syngas in the temperature range 900–1050 °C. Experiments were carried out with different ceria shapes via two-step redox cycling composed of endothermic partial reduction of ceria with methane and complete exothermic re-oxidation of reduced ceria with H_2O/CO_2 at the same operating temperature, thereby demonstrating the capability to operate the cycle isothermally. A parametric study considering different ceria macrostructure variants (ceria packed powder, ceria packed powder mixed with inert Al_2O_3 particles, and ceria reticulated porous foam) and operating parameters (methane flow-rate, reduction temperature, or sintering temperature) was conducted in order to unravel their impact on the bed-averaged oxygen non-stoichiometry (δ), syngas yield, methane conversion, and solar reactor performance. The ceria cycling stability was also experimentally investigated to demonstrate repeatable syngas production by alternating the flow between CH_4 and H_2O (or CO_2). A decrease in sintering temperature of the ceria foam was beneficial for increasing syngas selectivity, methane conversion, and reactor performance. Increasing both CH_4 concentration and reduction temperature enhanced δ with the maximum value up to 0.41 but concomitantly favored CH_4 cracking reaction. The ceria reticulated porous foam showed better performance in terms of effective heat transfer, due to volumetric absorption of concentrated solar radiation and uniform heating with lower solar power consumption, thereby promoting the solar-to-fuel energy conversion efficiency that reached up to 5.60%. The energy upgrade factor achieved during cycle was up to 1.19. Stable patterns in the δ and syngas yield for consecutive cycles with the ceria foam validated material performance stability.

1. Introduction

Concentrated solar power is a sustainable and desirable renewable-energy source for process heat to drive high-temperature thermochemical reactions, e.g. redox cycles. Of particular interest is solar energy conversion into transportable and dispatchable chemical fuels by water (H_2O) or carbon dioxide (CO_2) splitting using thermochemical redox cycles to produce syngas (mixture of hydrogen (H_2) and carbon monoxide (CO)). The resulting syngas can be further converted to liquid hydrocarbon fuel via Fischer–Tropsch [1] or utilized for production of methanol, ammonia, or dimethyl ether [2].

The conventional production of syngas through the conversion of methane (CH_4) involves steam reforming [3], dry reforming with CO_2 [4–7], and methane reforming over metal oxide redox materials [8–10] (partial oxidation of methane). The methane reforming over redox systems results in the partial oxidation of methane without the use of gaseous oxygen or catalysts and further allows operating the process as a cycle (because the solid oxide can be recycled back via oxidation with H_2O or CO_2) while producing syngas. The heat required for such an endothermic reaction can be provided by solar energy using concentrating solar power technologies, thereby converting solar energy into transportable and storable chemical fuels [11–14]. This two-step combined process

* Corresponding author.
E-mail address: stephane.abanades@promes.cnrs.fr (S. Abanades).

https://doi.org/10.1016/j.jechem.2019.05.004

(methane reforming and H_2O/CO_2 splitting) requires significantly lower reduction temperature as compared to the two-step oxide-based redox cycle [15,16] due to the aid of a reducing agent (CH_4). Since the metal oxide reduction with CH_4 and the H_2O/CO_2 splitting steps usually proceed at similar temperatures, isothermal cycle operation is made possible, which reduces the constrains imposed by reactor materials as well as thermal radiation losses [17].

The feasibility of utilizing metal oxides (either non-volatile or volatile metals) as oxygen carriers for CH_4 partial oxidation has been experimentally reported for ceria (CeO_2) [9,18], cerium-based oxides [8,19,20], iron oxide [21], tungsten oxide [13], and zinc oxide [11,22]. Among them, the partial oxidation of CH_4 with either doped or undoped ceria is particularly attractive owing to its capabilities for both rapid oxygen storage and release through lattice transfer, while retaining a stable crystallographic structure over a wide range of reduction extents [15], with reversible shift between Ce^{4+} and Ce^{3+} oxidation states [23,24].

Prior experimental study considering the partial oxidation of CH_4 using the redox properties of ceria was first reported by Otsuka et al. [9], without the utilization of solar energy. They demonstrated that the conversion of methane into syngas with a H_2/CO ratio of 2 was possible, and the reduced ceria could be re-oxidized with CO_2 to produce CO. Then, both thermodynamic and experimental studies [25,26] with the combination of concentrated solar energy were considered. Krenzke and Davidson [25] studied the thermodynamics of the ceria cycle with methane. They indicated that coupling the reduction of ceria with the partial oxidation of methane enables isothermal cycling at 950 °C with high-quality syngas produced during the reduction step and maximum predicted solar-to-fuel efficiency of 40%. Welte et al. [14] experimentally investigated the methane reforming over ceria in a particle-transport reactor. This reactor achieved a bed-averaged oxygen non-stoichiometry (δ) as high as 0.25 at the expense of unreacted ceria particle being entrained by the produced syngas.

The chemical-looping methane reforming over ceria can be represented by two steps. First, the endothermic partial ceria reduction in the presence of CH_4 that reacts with lattice oxygen for the production of syngas with a H_2/CO ratio of 2 suitable for methanol synthesis:

$$CeO_2 + \delta CH_4 \rightarrow CeO_{2-\delta} + \delta CO + 2\delta H_2 \quad (1)$$

Second, the oxidation of partially-reduced ceria with H_2O or CO_2:

$$CeO_{2-\delta} + \delta H_2O \rightarrow CeO_2 + \delta H_2 \quad (2)$$

$$CeO_{2-\delta} + \delta CO_2 \rightarrow CeO_2 + \delta CO \quad (3)$$

The advantages of the process combining partial oxidation of CH_4 and ceria redox cycle are: (i) the utilization of CH_4 in the reduction step allows for isothermal operation, thereby avoiding sensible heat losses taking place during temperature-swing cycle and eliminating the need for heat recovery, (ii) solid oxide is used in place of gaseous oxygen which eliminates the need for oxygen production from air, (iii) reduced ceria can be subsequently oxidized with either H_2O or CO_2 in an oxidation step to produce additional syngas and complete the cycle, (iv) deposited carbon on ceria structures can be concomitantly gasified and removed during the oxidation step, thus avoiding material deactivation and eliminating the requirement for expensive catalysts.

The ceria macrostructure plays a significant role on the performance of the combined two-step process in terms of conductive and radiative heat transfer across the material. Various metal oxide structures such as porous foams [15,16,26–29], textured plates [28], vertical pins [28], powder [30], powder mixed with inert material [23], multi-channeled honeycombs [31,32], felts [33], and three-dimensionally ordered macroporous (3DOM) ceramics [29,34] have been studied for two-step thermochemical H_2O/CO_2 splitting cycles in order to provide an effective interface for uniform concentrated solar energy absorption and sufficient surface area for supporting rapid chemical reactions. The powder bed structure or powder mixed with inert promoter [23] exhibited rapid oxidation rates; however at the expense of high radiative opacity, which may lead to undesired temperature gradients across the bed. Such a barrier can be tackled by using porous foam structures with high specific surface area [15,16], although heat transfer limitation may arise from their high optical thickness. Such reactive structures could therefore be applied advantageously to the solar-driven isothermal chemical looping reforming process with CH_4 and oxidant gas (H_2O or CO_2) alternately flowing through the oxide structure. Besides, different solar reactor concepts have been developed for thermochemical solar fuel production and applied to e.g. solar gasification or metal oxide redox cycles [35–41]. They can mainly be categorized as particle-based (encompassing packed or fluidized beds, entrained flows or particle clouds) or structured reactor technologies (volumetric porous receiver). However, versatile solar reactor operation applied to a large variety of ceria materials for methane reforming has not been considered to-date. The feasibility of isothermal solar-driven chemical looping methane reforming using ceria structures thus needs to be demonstrated in a flexible and scalable solar-operated reactor able to achieve both process steps continuously with repeatable fuel production, reversible oxygen exchange and thermochemical performance stability.

Therefore, because of the noticeable advantages of the methane reforming over ceria and the beneficial effects of ceria structures, the present study aims to investigate the chemical looping process with different ceria oxygen carrier structures in a novel flexible solar reactor driven by real high-flux concentrated solar power, provided by a parabolic dish solar concentrator. The whole process was reliably operated and demonstrated for the first time in this work under real solar irradiation conditions. The effect of different ceria structures (ceria reticulated porous foam, packed-bed ceria powder, and blend of ceria mixed with inert Al_2O_3 particles), CH_4 flow-rate, reduction temperature, and sintering temperature on the bed-averaged oxygen non-stoichiometry (δ), methane conversion, syngas production yield, and reactor performance was experimentally investigated and evaluated. A comprehensive experimental analysis of the solar process performance outputs was performed, encompassing quantification of gas yields produced during each step and by each side reaction, amounts of oxygen transferred during the redox process, as well as energy conversion efficiencies. Besides, cycling stability of the ceria structure for the combined two-step process performed in this solar reactor was also assessed.

2. Experimental

The solar reactor design and auxiliary components are schematically shown in Fig. 1. The solar reactor concept is based on a directly-irradiated packed-bed solar absorber configuration. The metallic cavity receiver is cylindrical with a conical shape (60° angle) at the cavity bottom (volume: 0.299 L and total height: 115 mm) and insulated by a 30 mm-thick alumino-silicate insulation layer. Its bottom is bored for the passage of an alumina tube (4 mm ext. diameter, 2 mm int. diameter) in which argon (Ar) carrier gas, and either CH_4 or H_2O/CO_2 are fed to react with ceria samples. The insulated cavity is vertically positioned in a water-cooled cylindrical stainless-steel shell. The top of the cavity is first closed by an alumina cap with a 20 mm-diameter aperture and then by a protective graphite layer (2 mm-thick) with a 15 mm-diameter aperture. The reactor front is lastly sealed by a hemispherical transparent glass window. A 2-m parabolic dish solar concentrator with a solar concentration ratio up to 10,551 suns

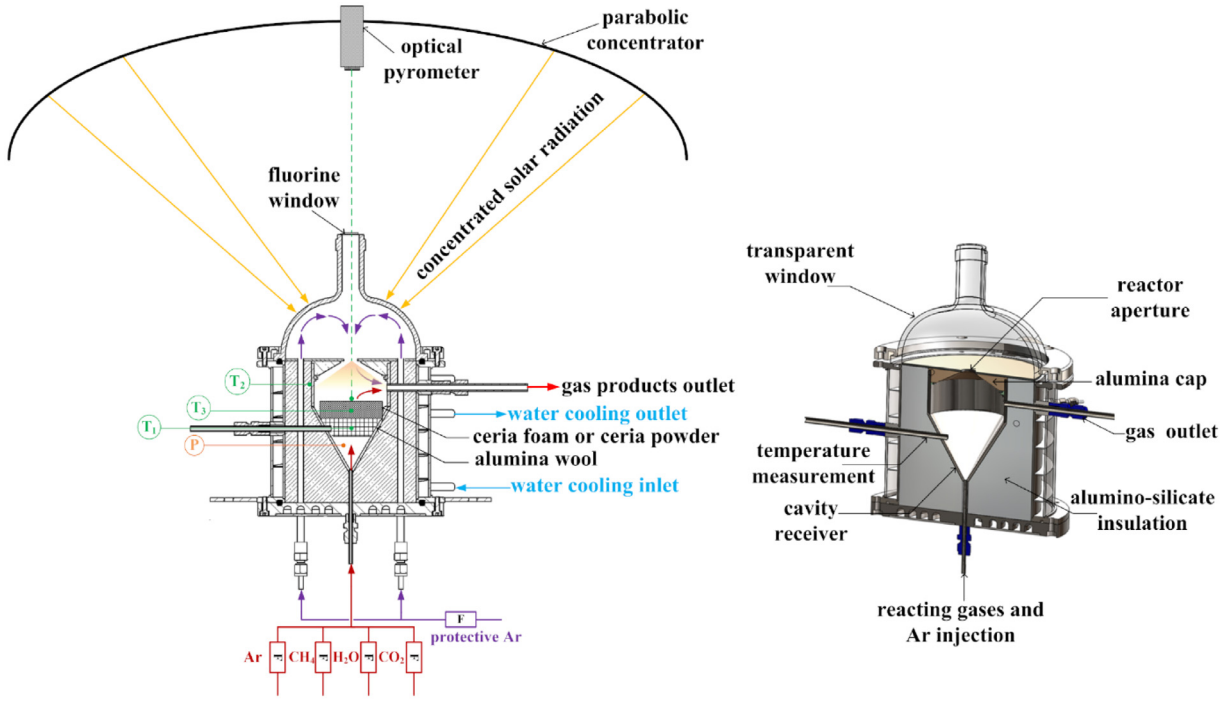

Fig. 1. Schematic of the 1.5 kW_{th} directly irradiated solar reactor and external components (left) and 3D cross section of the solar reactor (right).

(peak flux density of ~10.5 MW/m^2 for a DNI of 1 kW/m^2) is used to concentrate the solar radiation to the focal point.

Three temperatures are measured by B-type thermocouples inside the alumina wool (T_1), in the middle of ceria structure (T_3), and at the external cavity wall surface (T_2). An optical pyrometer (operating at 4.8–5.2 μm in a H_2O absorption band) is also utilized to directly measure the uppermost sample surface temperature through a fluorine window. The cavity pressure (P) is measured by a pressure transducer. Samples, either loose particles or foam (Fig. S1), are placed on the alumina wool support inside the cavity receiver directly exposed to concentrated solar irradiation. The ceria materials preparation is described in Supporting Information (materials synthesis). CH_4, CO_2, and Ar (gases purity of 99.999%) flow-rates are regulated by electronic Mass Flow Controllers (MFC, Brooks Instruments model SLA5850S, range 0–5 NL/min ±0.2% of full scale), and liquid water is also supplied by a MFC (range 0–30 g/h ± 1% of full scale). Reacting gases and Ar carrier gas are injected through the single inlet port at the cavity bottom. In addition, Ar protective gas is fed directly into the window area by two stainless tubes inserted in the insulation layer and subsequently enters the cavity via the aperture in the downward direction for preventing the hot gas contact with the transparent window. All the product gases with Ar exit the reactor via a single outlet port positioned at the upper cylindrical part of the cavity. They subsequently flow into a bubbler to condense steam and then through a gas filtering unit (two micro filters with 0.1 μm pore diameter) to remove moisture and solid carbon particles prior to gas analysis. Product syngas composition is monitored by an on-line syngas analyzer (GEIT 3100, uncertainty <±0.1% of full scale). Finally, all the measured data are recorded by an automated data acquisition system (BECKHOFF).

Experiments were performed at the focus of a vertical axis high-flux solar furnace of CNRS-PROMES, Odeillo. The reactor cavity was primarily flushed with Ar and simultaneously sucked by a Venturi pump to purge residual air from the system and maintain the pressure at ~0.9 bar (P_{atm}= ~0.85 bar at site elevation 1500 m above sea level). Subsequently, the reactor was progressively solar-heated to the targeted reduction temperature. The solar power input was controlled by means of shutter opening to adjust the operating temperature. During heating, the Ar carrier gas (0.2 NL/min) and Ar protective gas (2 NL/min) were supplied to the reactor cavity and window area, respectively. Figs. S2–S4 represent the evolution of temperatures and cavity pressure in the directly irradiated solar reactor during heating phase, ceria reduction with methane, and subsequent oxidation with H_2O at different operating cycle temperatures. While the cavity pressure remained stable (0.86 bar), the temperature increased gradually from the ambient temperature to the targeted temperature (1000 °C) for 35 min. It then changed in relation to endothermic and exothermic reactions and nominal operating cycle temperature defined, while the cavity pressure was constant (~0.9 bar) all over the cycles. According to Fig. S2, the homogeneous temperature inside the ceria foam as well as the reactor cavity receiver was confirmed by narrow gaps between T_1 (below the foam), T_3 (inside the foam), and $T_{pyrometer}$ (upper surface of the foam) while the external cavity wall temperature (T_2) was ~150 °C lower than those temperatures.

After reaching the desired reduction temperature, the CH_4 flow-rate was delivered along with Ar carrier gas to drive the reduction reaction, and it was then stopped when H_2 and CO concentrations approached zero. Subsequently, ceria oxidation was performed by injecting the reacting gases (either H_2O or CO_2) at the same temperature. The produced syngas was continuously analyzed, and the flow rate of each gas specie (F_i) was calculated from their measured mole fraction (y_i) and the known inlet flow rate of Ar (F_{Ar}): ($F_i = F_{Ar} \cdot y_i/y_{Ar}$). Then, the averaged oxygen non-stoichiometry in ceria (δ) and syngas yields were quantified by time-integration of the measured gas production rates over each cycle. The performance metrics of the solar reactor were determined from the measured gas production and solar power input.

In the first step, during partial oxidation of methane with ceria, the reaction of CH_4 with excess surface oxygen is also possible (especially at the beginning of the reaction when the amount of surface oxygen is maximum), then leading to the formation of H_2O and CO_2 (by the following reaction: $4CeO_2+\delta CH_4 \longrightarrow 4CeO_{2-\delta}+\delta CO_2+2\delta H_2O$). Thus, oxygen is recovered in the forms of CO, CO_2, and H_2O (twice the amount of CO_2).

Therefore, the oxygen non-stoichiometry (δ_{red}) can be determined by:

$$\delta_{red}=\frac{n_{CO}+2n_{CO_2}+n_{H_2O}}{n_{CeO_2}} \quad (4)$$

where n_i are the mole amounts of species i.

The replenished oxygen (δ_{ox}) during ceria oxidation with H_2O (Eq. (2)) can be calculated from the total amount of produced H_2 from which the amounts of H_2 produced by the reactions of carbon with H_2O are subtracted ($C+H_2O\longrightarrow CO+H_2$ and $C+2H_2O\longrightarrow CO_2+2H_2$):

$$\delta_{ox}=\frac{n_{H_2}-n_{CO}-2n_{CO2}}{n_{CeO_2}} \quad (5)$$

When using CO_2 as oxidant (Eq. (3)), the replenished oxygen (δ_{ox}) is calculated by the mass balance of oxygen:

$$\delta_{ox}=\frac{2n_{CO_{2,in}}-n_{CO,out}-2n_{CO_{2,out}}}{n_{CeO_2}} \quad (6)$$

The performance metrics of the solar reactor for the chemical-looping process are encompassing methane conversion, solar-to-fuel energy conversion efficiency, and energy upgrade factor.

The solar-to-fuel energy conversion efficiency ($\eta_{solar\text{-}to\text{-}fuel}$) is defined as the ratio of the total chemical energy content of the produced syngas to the total energy input (including solar power input in both the reduction and oxidation steps and heating value of the converted methane):

$$\eta_{solar-to-fuel}=\frac{(\dot{m}_{H_2}\cdot LHV_{H_2}+\dot{m}_{CO}\cdot LHV_{CO})_{cycle}}{\dot{P}_{solar}+(X_{CH_4}\cdot\dot{m}_{CH_4}\cdot LHV_{CH_4})} \quad (7)$$

where LHV represents the Lower Heating Value (J/kg), $\dot{m}_{H_2}$ and $\dot{m}_{CO}$ the mass flow rates of H_2 and CO produced in the cycle (kg/s) $\dot{m}_{CH_4}$ the mass flow rate of injected methane, $\dot{P}_{solar}$ the total solar power input in the cycle (W), and X_{CH_4} the methane conversion ($X_{CH_4}=1-\frac{\dot{m}_{unreacted\ CH_4}}{\dot{m}_{CH_4}}$).

The energy upgrade factor (U) is obtained by the ratio of the energy contained in the outlet gas species to the energy content of the inlet flow:

$$U=\frac{(\dot{m}_{H_2}\cdot LHV_{H_2}+\dot{m}_{CO}\cdot LHV_{CO})_{cycle}+((1-X_{CH_4})\cdot m_{CH_4}\cdot LHV_{CH_4})}{(\dot{m}_{CH_4}\cdot LHV_{CH_4})} \quad (8)$$

All the operating conditions and experimental results for 44 runs with 6 different ceria samples performed in the solar reactor are summarized in Supporting Information (Table S1).

3. Results and discussion

3.1. Influence of sintering temperature for ceria foams

In order to experimentally study the effect of calcination temperature during ceria foam elaboration on the evolved syngas yield, two ceria reticulated porous foams were prepared and subsequently annealed under air at 1000 °C (for 6 h) and one of them was further sintered at 1400 °C (for 2 h) for densifying the structure. Thus, the obtained sintered foams were labeled as ST-1000 and ST-1400, respectively. The initial volumes of ST-1000 and ST-1400 were 46.76 and 83.13 cm^3 (after ceria coating process), and they were shrunk to 30.88 cm^3 (Fig. S5a, ST-1000) and 31.10 cm^3 (Fig. S5b, ST-1400) after heat treatment, representing a decrease of 34% and 63% of their initial volume, respectively. The final properties of the ceria foams are: porosity: 91.8% and 89.1%, mean cell size: 3.5 and 2.5 mm, and apparent density: 0.595 and 0.780 g/cm^3 for ST-1000 and ST-1400, respectively.

Both ceria foams were cycled in the temperature range 900–1050 °C to experimentally study the influence of temperature on syngas evolution as well as reactor performance. Fig. S6 shows the syngas production rates along with nominal reactor temperature during ceria foam (ST-1400) reduction in the range 900–1050 °C (CH_4 flow-rate: 0.2 NL/min, Ar flow rate: 0.2 NL/min, 50% CH_4 mole fraction). It was followed by subsequent ceria oxidation with H_2O carried out at the same temperature (H_2O: 200 mg/min, Ar: 0.2 NL/min, 55% steam mole fraction at inlet).

During reduction step, CO_2 production rate was maximal at the initial stage of the reaction, and it increased with temperature. In fact, H_2O was also formed simultaneously [9,10,42]; however, it cannot be detected from gas analysis. An increase in the operating cycle temperature promoted both the syngas production rate (especially H_2 and CO) and ceria reduction rate (as evidenced by a shortened reaction duration). The peak rates of CO and H_2 produced were 0.02 and 0.04 NL/min at 900 °C compared to 0.11 and 0.24 NL/min at 1050 °C, and the operating duration was 25.4 min at 900 °C compared to 18.4 min at 1050 °C. It is interesting to note that the H_2/CO mole ratio is constantly ~2 for any reduction temperatures [9]. Moreover, the significant H_2 evolution still continuing after 12 min (Fig. S6e) was the result of the methane cracking reaction that is thermodynamically favorable at high temperature (>1000 °C) [23].

During oxidation step, the H_2 production rate increased with temperature while the CO and CO_2 production rates were negligible over the considered temperature range, thus demonstrating negligible impact of carbon formation associated with methane cracking for ST-1400.

Fig. 2 compares the H_2, CO, and CO_2 production rates (both reduction and oxidation steps) of ceria foam ST-1400 to those of ST-1000 at an operating cycle temperature of 1000 °C. During reduction step (Fig. 2a), increasing the sintering temperature (ST-1400) decreased syngas production rates while increasing the operating duration. This is because the high densification of the structure (at high sintering temperature of 1400 °C) leads to a decline of the porosity and hinders the access of the reacting gas to the solid surface and hollow struts of the foam. Likewise, higher sintering temperature (ST-1400) also led to lower reaction rates during oxidation step (Fig. 2b). Decreasing the sintering temperature (ST-1000) favored the oxidation rate and the formation of CO/CO_2 (because the formation of carbon during the reduction step was also favored).

Fig. 3 presents the comparison of syngas yields (calculated by time-integration of the measured syngas production rates) produced per gram of CeO_2 ($mmol/g_{CeO_2}$) between ST-1000 and ST-1400 at the operating cycle temperatures of 1000 and 1050 °C during ceria reduction with CH_4 (Fig. 3a) and oxidation with H_2O (Fig. 3b). The syngas yields ascribed to the main reactions (Eqs. (1) and (2)) and side reactions (methane cracking during reduction step: $CH_4\longrightarrow C+2H_2$, and carbon gasification during oxidation step: $C+H_2O\longrightarrow CO+H_2$ and $C+2H_2O\longrightarrow CO_2+2H_2$) are presented separately.

Fig. 3(a) shows that the syngas yields produced during reduction step decreased significantly with sintering temperature at the operating cycle temperatures of 1000 and 1050 °C, thus leading to a decline in δ_{red} (e.g., from 0.36 for ST-1000 to 0.34 for ST-1400 at 1000 °C). Furthermore, the H_2 yield produced from CH_4 cracking reaction (quantified by the total H_2 yield measured by gas analysis minus the H_2 yield produced by the reaction of ceria with methane, which is equivalent to twice the quantity of produced CO, according to Eq. (1)) decreased considerably when increasing the sintering temperature (e.g. from 0.67 $mmol/g_{CeO_2}$ for ST-1000 to 0.07 $mmol/g_{CeO_2}$ for ST-1400 at 1000 °C). This can be explained by the fact that increasing the sintering temperature lowers the available geometrical surface area for the heterogeneous reaction,

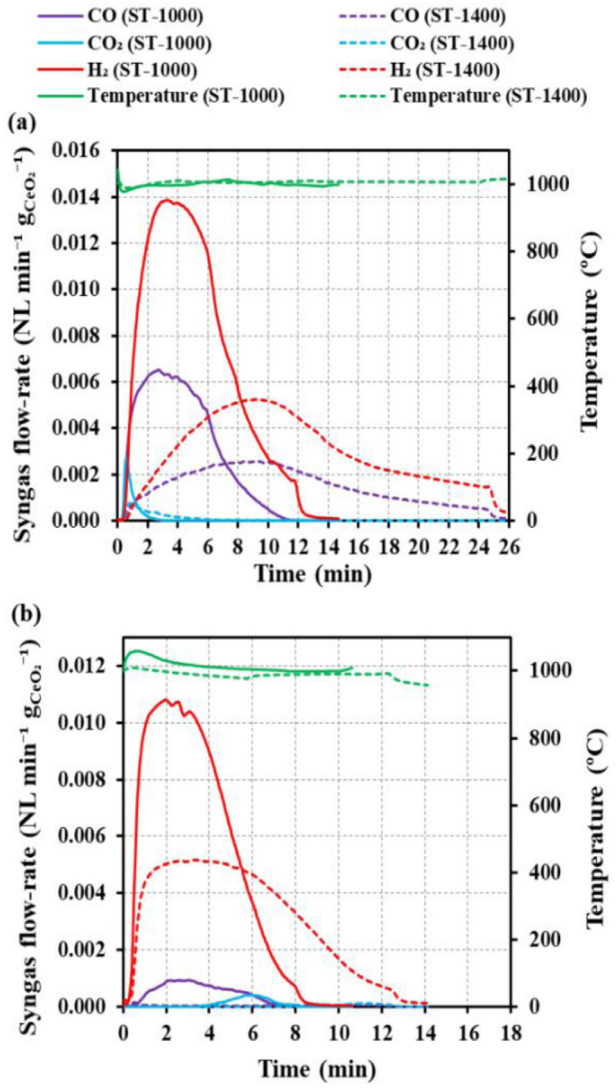

Fig. 2. Influence of sintering temperature on H_2 and CO production rates during both reduction and oxidation of ceria foam at 1000 °C: (a) CH_4 was utilized as reducing agent and (b) H_2O was utilized as oxidizing agent.

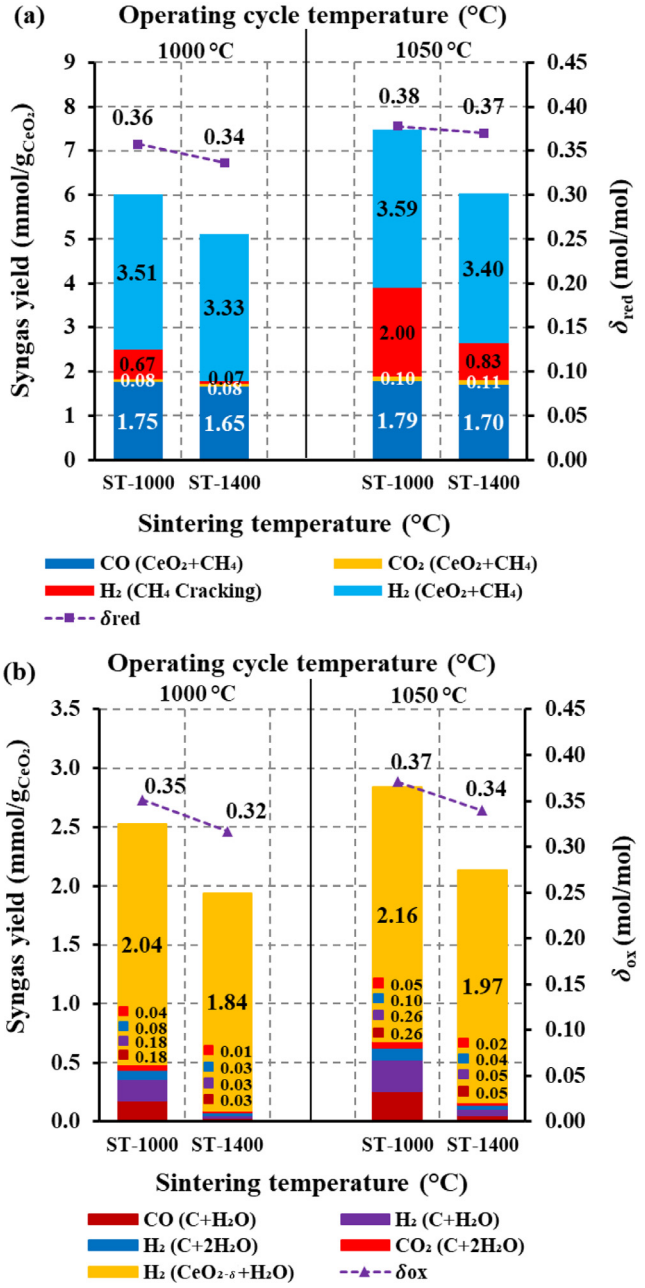

Fig. 3. Effect of sintering temperature and cycle operating temperature on syngas yields, δ_{red}, and δ_{ox} for (a) reduction and (b) oxidation of ceria foam cycled isothermally at a CH_4 flow-rate of 0.2 NL/min.

which declines the surface concentration of adsorbed methane and alleviates the methane cracking reaction.

Likewise, Fig. 3(b) confirms that the methane cracking reaction is not favored for the sintered ceria foam (ST-1400), as evidenced by a sharp drop in the quantities of CO ($C+H_2O$), CO_2 ($C+2H_2O$), H_2 ($C+H_2O$), and H_2 ($C+2H_2O$) formed by the side reactions (carbon deposit gasification with H_2O). Note that the H_2 ($C+H_2O$) yield is equal to the CO yield measured by gas analysis ($C+H_2O \longrightarrow CO+H_2$), while the H_2 ($C+2H_2O$) yield is equal to twice the CO_2 yield measured by gas analysis ($C+2H_2O \longrightarrow CO_2+2H_2$). In addition, an increase in the sintering temperature decreased the H_2 ($CeO_{2-\delta}+H_2O$) yield (e.g., from 2.04 mmol/g_{CeO_2} for ST-1000 to 1.84 mmol/g_{CeO_2} for ST-1400 at 1000 °C, thus resulting in a decrease of δ_{ox} from 0.35 to 0.32). Noticeably, δ_{red} matched well δ_{ox} values at both cycle temperatures of 1000 and 1050 °C, thereby confirming complete re-oxidation.

According to Fig. 4(a), the reduction yield ($X_{red}=\delta_{red}/\delta_{max}$ where $\delta_{max}=0.5$ for complete reduction of Ce^{4+} into Ce^{3+}), oxidation yield ($X_{ox}=\delta_{ox}/\delta_{red}$), methane conversion ($X_{CH_4}$) and solar-to fuel energy conversion efficiency ($\eta_{solar\text{-}to\text{-}fuel}$) were decreased when increasing the sintering temperature (e.g., X_{red}, X_{ox}, X_{CH_4}, and $\eta_{solar\text{-}to\text{-}fuel}$ ranging from 71.5%, 98.3%, 46.9%, and 3.8% for ST-1000 to 67.3%, 94.2%, 23.0%, and 2.8% for ST-1400, respectively, during cycling at 1000 °C). In addition, an increase in operating cycle temperature enhanced X_{red}, X_{CH_4}, and $\eta_{solar\text{-}to\text{-}fuel}$.

Fig. 4(b) compares the total syngas yields obtained for both reduction and oxidation steps of ceria foams (ST-1000 compared to ST-1400) during cycling at 1000 and 1050 °C. Increasing sintering temperature considerably decreased total H_2 and CO yields (from 6.48 and 1.93 mmol/g_{CeO_2} for ST-1000 to 5.29 and 1.68 mmol/g_{CeO_2} for ST-1400, respectively, at 1000 °C); however, the CO_2 and H_2O yields tended to decrease slightly. A growth in the energy upgrade factor (U) with increasing sintering temperature was observed (e.g., from 1.03 for ST-1000 to 1.08 for ST-1400). This is because a high sintering of the ceria foam lowers the gaseous reactant access to the reactive surface and the ceria bulk reduction, thus increasing the unreacted CH_4 (much lower X_{CH_4} for ST-1400, Fig. 4a) and

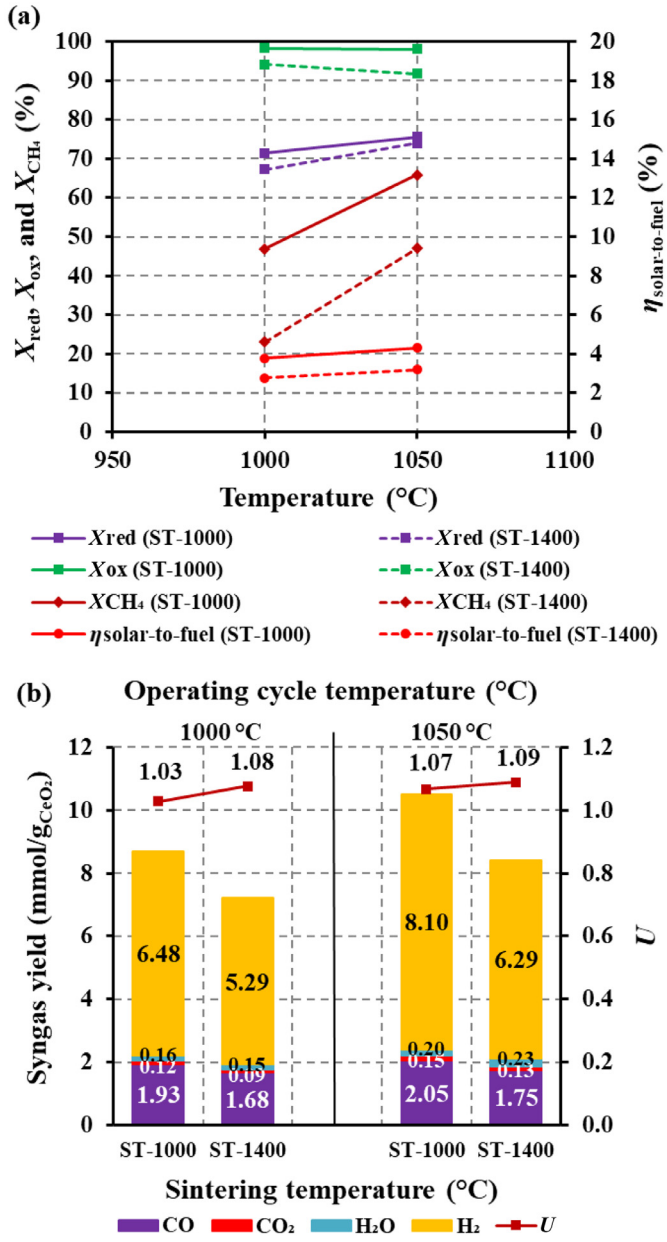

Fig. 4. Effect of sintering temperature and cycle operating temperature on (a) ceria reduction yield, ceria oxidation yield, methane conversion, and solar-to-fuel energy conversion efficiency, and (b) energy upgrade factor and total syngas yields obtained from both reduction and oxidation steps.

thereby leading to an increase in *U*. From these observations, it can be summarized that decreasing sintering temperature enhanced syngas production, however at the expense of weakened structure, with reduced thermo-mechanical resistance.

3.2. Influence of methane flow-rate and ceria macrostructure on syngas yield

The impact of methane flow-rate on syngas yields was experimentally studied with different ceria structures. Three ceria structures consisting of pure ceria powder (25.0052 g, bulk density: 1.12 g/cm^3, loose bed porosity: 84.5%), ceria powder (27.0605 g) mixed with inert Al_2O_3 promoter (bulk mixture density: 1.53 g/cm^3, loose bed porosity: 69.1%), and ceria reticulated foam (18.3705 g, ST-1000, bulk density: 0.595 g/cm^3, porosity: 91.8%) were employed to investigate the influence of ceria structure and reactive bed layout on syngas yield and reactor performance. During ceria reduction step, the CH_4 flow-rate was injected at 0.1, 0.2, 0.3 and 0.4 NL/min (with constant Ar carrier flow of 0.2 NL/min) at 1000 °C. In the oxidation step performed at the same temperature (1000 °C), H_2O was delivered at a constant flow-rate of 200 mg/min (with Ar carrier gas flow of 0.2 NL/min).

Fig. 5 shows the influence of CH_4 flow rate on syngas yields for each ceria structure. According to Fig. 5(a), the H_2 and CO yields first increased significantly within a CH_4 flow-rate range of 0.1–0.2 NL/min and then tended to grow minimally at above 0.2 NL/min. For example, the H_2 and CO yields for ceria foam rose from 3.25 and 1.66 mmol/g_{CeO_2} at 0.1 NL/min to 3.64 and 1.82 mmol/g_{CeO_2} at 0.2 NL/min, and 3.78 and 1.89 mmol/g_{CeO_2} at 0.4 NL/min. The CO_2 yields for each ceria structure remained stable in negligible amounts (0.05–0.10 mmol/g_{CeO_2} within the considered range). A plateau in the H_2 and CO (at CH_4 above 0.2 NL/min) indicates that the final state completion of ceria reduction for each ceria structure is being approached, thereby leading to an excess in CH_4 flow-rate supply, which in turn favors CH_4 cracking reaction. Note that if the rate of ceria reduction is lower than the rate of methane decomposition, chemisorbed carbon may accumulate at the surface. This occurs when the rate of bulk lattice oxygen diffusion to the surface becomes lower than the CH_4 supply rate. In other words, when a lack of oxygen at the surface occurs, then carbon deposition is fastened, which is increasingly favored as oxygen is being depleted during the ceria reduction progress. It is interesting to highlight that when accounting for H_2 produced by CH_4 cracking reaction (Fig. 5b), the H_2 yield increased steeply (3.25–6.54 mmol/g_{CeO_2} for ceria foam) over the considered range, thus confirming that the CH_4 cracking reaction is favored when increasing CH_4 flow-rate, and leading to a sharp increase in H_2 yield along with carbon deposition.

The CO and H_2 productions for each ceria structure were not significantly different, although a slightly higher H_2 and CO production was noticed for ceria powder (presumably due to non-uniform heating of the bed ($T_{pyrometer} > T_3$) as evidenced by Fig. S3 for ceria powder and Fig. S4 for ceria powder mixed with inert Al_2O_3 promoter). This advantageously confirms that the shaping of ceria as foam does not downgrade the reactivity.

During subsequent ceria oxidation with H_2O at 1000 °C (Fig. 5c,d), H_2 yield (produced by Eq. (2)) increased in accordance with an increase in CH_4 flow-rate during the reduction step, while the CO and CO_2 yields (produced by side reactions) also rose due to carbon deposition increase (Fig. 5c). For instance, the yields of H_2, CO, and CO_2 for ceria foam were 2.01, 0.11, and 0.01 mmol/g_{CeO_2} at 0.1 NL/min compared to 2.16, 0.20, and 0.04 mmol/g_{CeO_2} at 0.4 NL/min. Likewise, the H_2 yield increased sharper when including the amount of H_2 associated with carbon gasification (e.g. from 2.14 to 2.45 mmol/g_{CeO_2} at 0.1–0.4 NL/min for ceria foam), according to Fig. 5(d). However, no significant effect of the ceria structure on H_2, CO, and CO_2 yields can be evidenced whether or not accounting for H_2 yields from carbon gasification reactions.

In order to emphasize the influence of CH_4 flow-rate on reactor performance, the evolution of the relevant metrics (δ_{red} and δ_{ox}, X_{red}, X_{ox}, X_{CH_4}, *U*, and $\eta_{solar\text{-}to\text{-}fuel}$) is presented in Fig. 6. Both δ_{red} (Fig. 6a) and δ_{ox} (Fig. 6b) are enhanced with a CH_4 flow-rate increase (e.g., maximum δ_{red} and δ_{ox} of 0.41 and 0.39 at 0.4 NL/min, respectively, for ceria powder). Besides, the δ_{ox} values were consistent with δ_{red} for any ceria structures, thereby confirming complete ceria re-oxidation with H_2O. As expected, the δ_{red} (Fig. 6a) of ceria powder (0.37–0.41) was slightly higher than those of other materials, in agreement with the higher syngas yields during reduction (Fig. 5a). The δ_{ox} values were not different (Fig. 6b) (0.34–0.39 for ceria powder and 0.35–0.37 for ceria reticulated foam), in agreement with the similar syngas yields

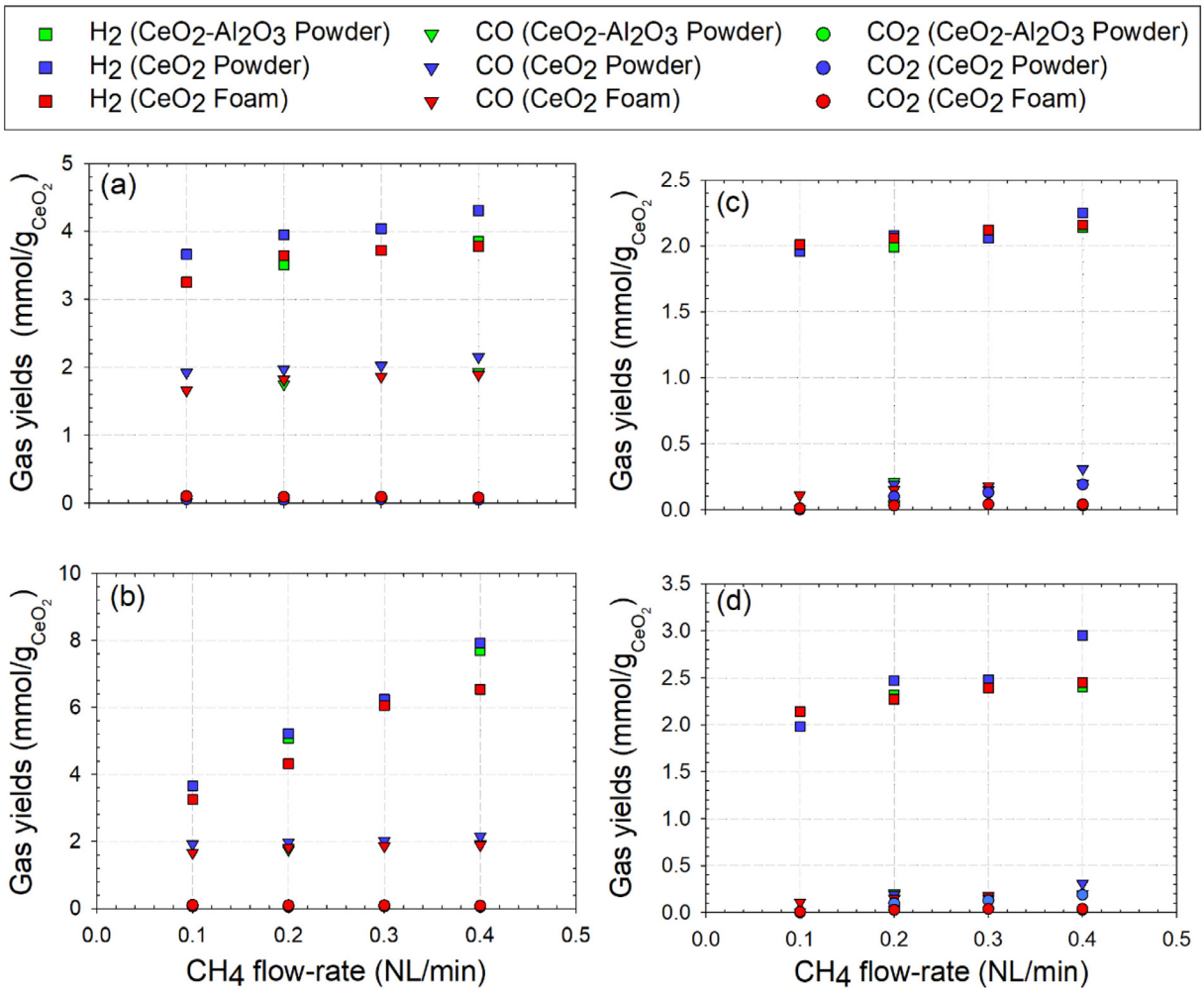

Fig. 5. Effect of CH_4 flow-rate on H_2, CO, and CO_2 yields during (a, b) reduction of different ceria structures at 1000 °C: (a) not accounting and (b) accounting for H_2 produced by CH_4 cracking reaction; and during (c, d) oxidation of different ceria structures with H_2O at 1000 °C: (c) not accounting and (d) accounting for H_2 produced by carbon gasification reactions.

during oxidation (Fig. 5c). X_{red} grew with increasing CH_4 flow-rate (Fig. 6c), e.g. from 74.7% at 0.1 NL/min to 81.3% at 0.4 NL/min for ceria powder, and no significant influence of ceria structure on X_{red} can be observed. X_{ox} values were close to ~100% for any ceria structures, thereby demonstrating complete ceria re-oxidation. X_{CH_4} was reduced noticeably with increasing CH_4 flow-rate for each ceria structure (Fig. 6d) (e.g., from 76.4% to 43.0% at 0.1–0.4 NL/min, respectively, for ceria powder). The decrease in X_{CH_4} is attributable to the CH_4 supply rate that exceeds the rate of oxygen released by ceria, as noticed by a stable profile in X_{red} at 0.3–0.4 NL/min (Fig. 6c). U tended to decrease with CH_4 flow-rate (Fig. 6e). This variation is attributed to the carbon formation increase with CH_4 flow-rate, and partial entrainment out of the reactor cavity, as confirmed by the presence of carbon particles in the filtering unit (Fig. S7), thus losing their heating value and lowering U. As expected, $\eta_{solar\text{-}to\text{-}fuel}$ rose with CH_4 flow-rate as a result of the substantial syngas yield improvement (Fig. 5), and the highest $\eta_{solar\text{-}to\text{-}fuel}$ was obtained for ceria foam (3.1%–5.6%), followed by CeO_2–Al_2O_3 blend (3.6%–5.0%), and CeO_2 powder (3.1%–3.6%), according to Fig. 6(f). This can be explained by the different solar power inputs required for different ceria structures (1.06–1.14 kW for ceria powder, followed by 0.96–1.06 kW for CeO_2–Al_2O_3 blend, and 0.76–0.86 kW for ceria foam at 1000 °C). Ceria foam thus requires lower solar power consumption than CeO_2–Al_2O_3 blend and CeO_2 powder. This is because the CeO_2–Al_2O_3 blend stands out from its high bed thickness (1.19 cm) and additional Al_2O_3 heating (Fig. S8), while the CeO_2 powder layer (0.46 cm thickness) shows high opacity, which is not suitable for efficient radiative heat transfer in the whole volume. Both issues thus lead to temperature gradient, as evidenced in both Fig. S3 (for CeO_2 powder) and Fig. S4 (for CeO_2–Al_2O_3 blend), with a higher temperature at the bed uppermost surface ($T_{pyrometer} > T_3$). However, the CeO_2–Al_2O_3 blend offers a favored dispersion of ceria powder, which improves the gas flow through the reactive bed and heat transfer, and promotes the syngas yield (thereby leading to higher $\eta_{solar\text{-}to\text{-}fuel}$ than for ceria powder). The ceria foam consumed the lowest solar power input (thus enhancing $\eta_{solar\text{-}to\text{-}fuel}$), arising from the effective heat transfer through the semi-transparent medium and the uniform heating (as evidenced by the narrow temperature gap between ceria surface $T_{pyrometer}$ and T_3 in Fig. S2). In summary, the ceria foam structure is the most efficient in term of heat transfer (as reflected by uniform heating with lower solar power consumption), thereby leading to higher $\eta_{solar\text{-}to\text{-}fuel}$, and it is thus the most suitable for the chemical-looping methane reforming.

3.3. Influence of temperature on syngas yield

The influence of temperature on syngas yield was investigated for the different ceria structures at 900, 950, 1000, and 1050 °C (T_3 is the nominal-mentioned temperature for experiments).

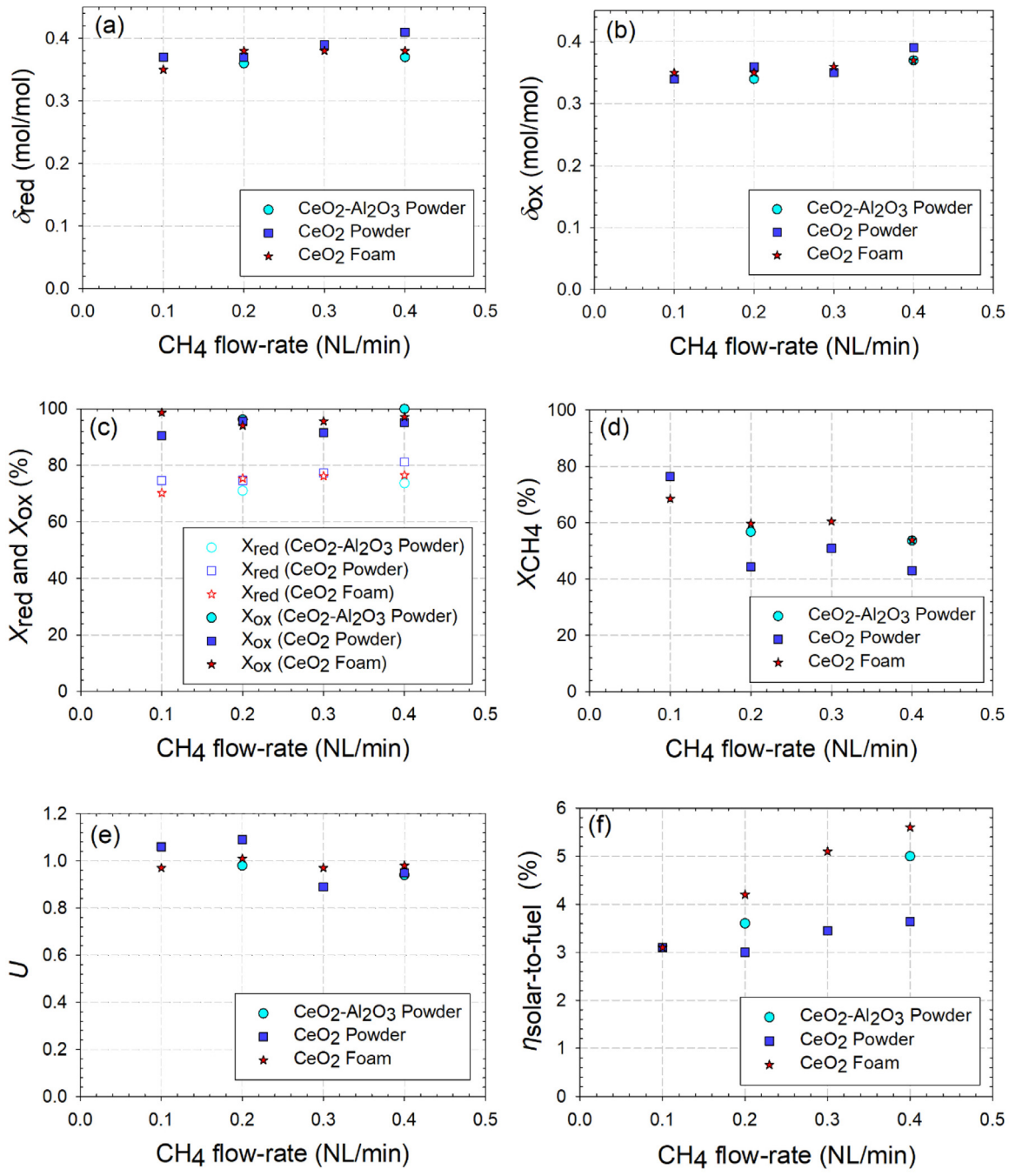

Fig. 6. Effect of CH_4 flow-rate on (a) δ_{red}, (b) δ_{ox}, (c) reduction yield (X_{red}) and oxidation yield (X_{ox}), (d) CH_4 conversion (X_{CH_4}), (e) energy upgrade factor (U), and (f) solar-to-fuel energy conversion efficiency ($\eta_{solar\text{-}to\text{-}fuel}$) for different ceria structures at 1000 °C.

Fig. 7(a) and (b) shows the H_2, CO, and CO_2 yields obtained from ceria reduction with CH_4 as a function of reduction temperature. As expected, both H_2 and CO yields increased sharply, while CO_2 tended to rise minimally with temperature (Fig. 7a), regardless of the ceria structures. For example, H_2, CO, and CO_2 yields rose from 2.38, 1.21, and 0.05 mmol/g_{CeO_2} at 900 °C to 3.84, 1.92, and 0.09 mmol/g_{CeO_2} at 1050 °C, respectively, for CeO_2–Al_2O_3 blend. This is because increasing temperature accelerates the kinetic rate of ceria reduction with faster oxygen release, as evidenced by Arrhenius plot (Fig. S9). The activation energy obtained for each ceria structure (92.8–114.2 kJ/mol for H_2 and 92.8–95.1 kJ/mol for CO, Table. S2) is consistent with previously reported data [23]. When accounting for the H_2 produced by CH_4 cracking reaction (Fig. 7b), the trends of H_2 became steeper, thus pointing out the significant influence of the reduction temperature on the H_2 formation from CH_4 cracking. Noticeably, the H_2 yield at 900 °C (CeO_2–Al_2O_3 blend) remained the same (2.38 mmol/g_{CeO_2}) whether or not accounting for H_2 produced by cracking reaction, thus indicating that CH_4 decomposition was negligible at 900 °C. In comparison, the ceria powder showed the highest H_2 and CO yields at 950–1000 °C, as a result of the higher bed surface temperature and lower bed height, as previously mentioned.

Fig. 7(c) and (d) depicts the H_2, CO, and CO_2 yields measured during ceria oxidation with H_2O as a function of temperature. The H_2 yields (from Eq. (2)) rose significantly with temperature (1.39–2.12 mmol/g_{CeO_2} for CeO_2–Al_2O_3 blend), while a slight increase in CO and CO_2 yields was noticed (Fig. 7c). The presence of CO and CO_2 (e.g., ranging between 0.06 and 0.23 mmol/g_{CeO_2}

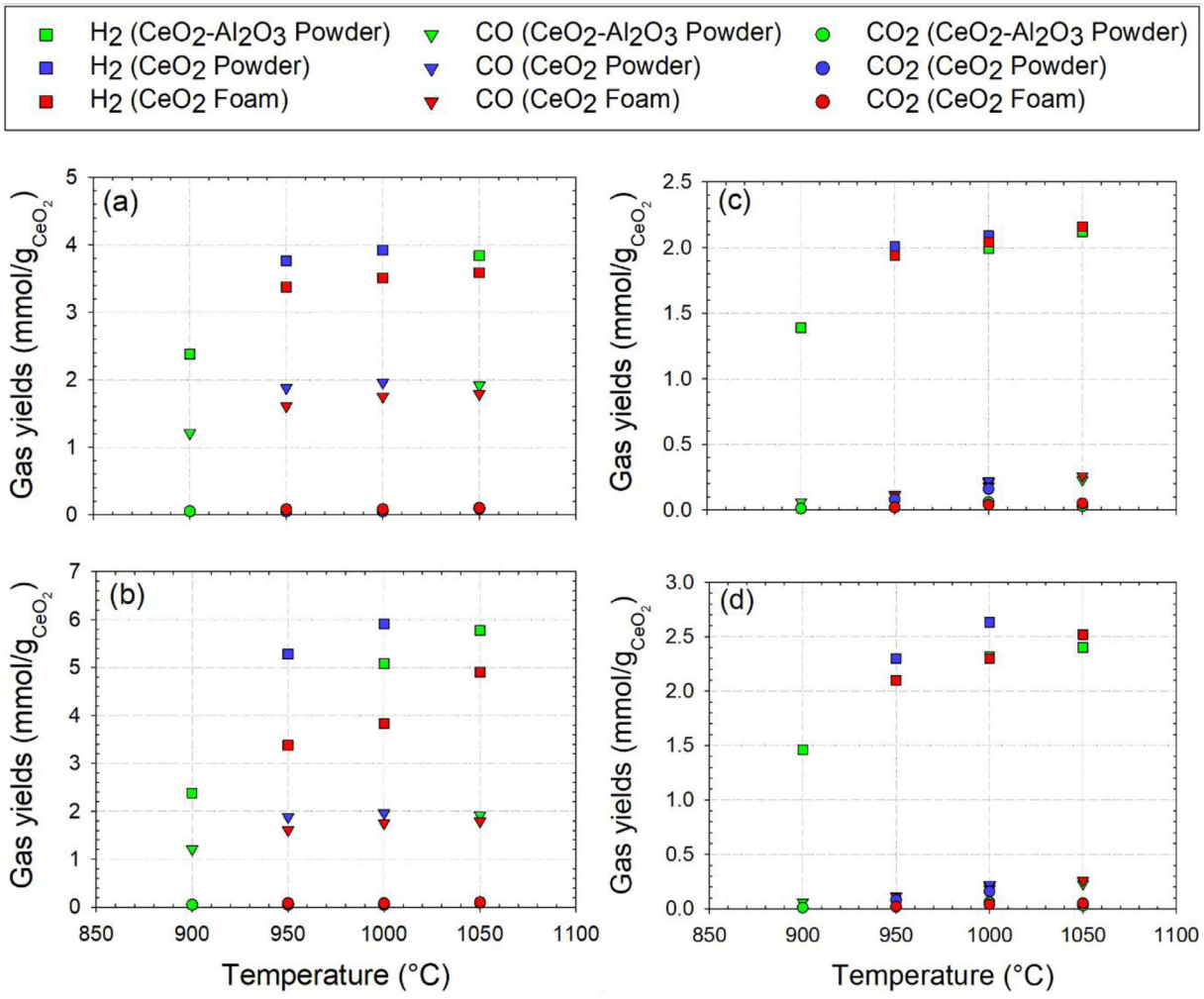

Fig. 7. Effect of temperature on H_2, CO, and CO_2 yields during (a, b) ceria materials reduction with CH_4 (0.2 NL/min, inlet CH_4 mole fraction: 50%): (a) not accounting and (b) accounting for H_2 produced by CH_4 cracking reaction; and during (c, d) ceria materials oxidation with H_2O (200 mg/min, inlet steam mole fraction: 55%): (c) not accounting and (d) accounting for H_2 produced by carbon gasification reactions.

for CO and 0.01 and 0.03 mmol/g_{CeO_2} for CO_2 in the case of CeO_2–Al_2O_3 blend) is attributed to the side reactions of carbon gasification forming additional H_2, CO, and CO_2. These side reactions are beneficial to eliminate the deposited carbon on the surface of ceria structure, thereby avoiding deactivation. When including the H_2 produced by the carbon gasification (Fig. 7d), the H_2 yield for each ceria structure was higher (1.46–2.40 mmol/g_{CeO_2} for CeO_2–Al_2O_3 blend), thus confirming the growing effect of temperature on carbon formation.

Fig. 8 presents the evolution of δ_{red}, δ_{ox}, X_{red}, X_{ox}, X_{CH_4}, U, and $\eta_{solar\text{-}to\text{-}fuel}$ as a function of temperature for each ceria structure. The temperature increase improved steadily the reduction extent of ceria δ_{red} (Fig. 8a), e.g. from 0.24 at 950 °C to 0.39 at 1050 °C for CeO_2–Al_2O_3 blend owing to a significant beneficial enhancement of the reduction kinetics (Fig. S9). δ_{ox} also increased with temperature (ranging between 0.24 and 0.36 for CeO_2–Al_2O_3 blend, Fig. 8b) due to the oxygen vacancies consistently increasing with temperature. The impact of the considered ceria structures on both δ_{red} and δ_{ox} was not significant. δ_{ox} values were similar to δ_{red} values, thus validating complete ceria re-oxidation for any ceria structures. X_{red} rose considerably with temperature (e.g., in the range 48.8–78.0% for CeO_2–Al_2O_3 blend), while X_{ox} remained quite constant at ~100% for any ceria structures (Fig. 8c), thereby confirming complete ceria re-oxidation. X_{CH_4} rose with temperature (Fig. 8d), and the highest X_{CH_4} was attained at 1050 °C (77.4% for CeO_2–Al_2O_3 blend). This is because the faster rate of oxygen release better matched the constant inlet flow of CH_4, which leads to X_{CH_4} increase. The X_{CH_4} for both ceria foam and CeO_2–Al_2O_3 blend was higher than that of ceria powder, presumably due to both better gas flow through the structure and solid/gas contact between ceria and CH_4. Moreover, U (Fig. 8e) first increased slightly within 900–950 °C and then decreased above 950 °C, as a result of carbon formation issue. Indeed, the carbon deposition increased with increasing temperature, and some particles escaped from the reactor cavity via gas flow, thus lowering U. This issue can be tackled by decreasing temperature to favor U at the expense of lower syngas yield. $\eta_{solar\text{-}to\text{-}fuel}$ (Fig. 8f) was improved by increasing temperature (e.g., in the range of 3.0%–4.3% for ceria foam). The lowest $\eta_{solar\text{-}to\text{-}fuel}$ values were observed for ceria powder (2.75%–2.97% at 950–1000 °C) because of the higher solar power consumption (0.88–0.96 kW for ceria powder compared to 0.67–0.68 kW for ceria foam in the temperature range 950–1000 °C), confirming that ceria foam structure is the most suitable for the solar combined process.

3.4. Oxidation step with CO_2 during ceria cycling

Another ceria powder (27.0892 g) mixed with Al_2O_3 (50 g) was employed to study the influence of temperature (950–1050 °C) on syngas yield and reactor performance during ceria

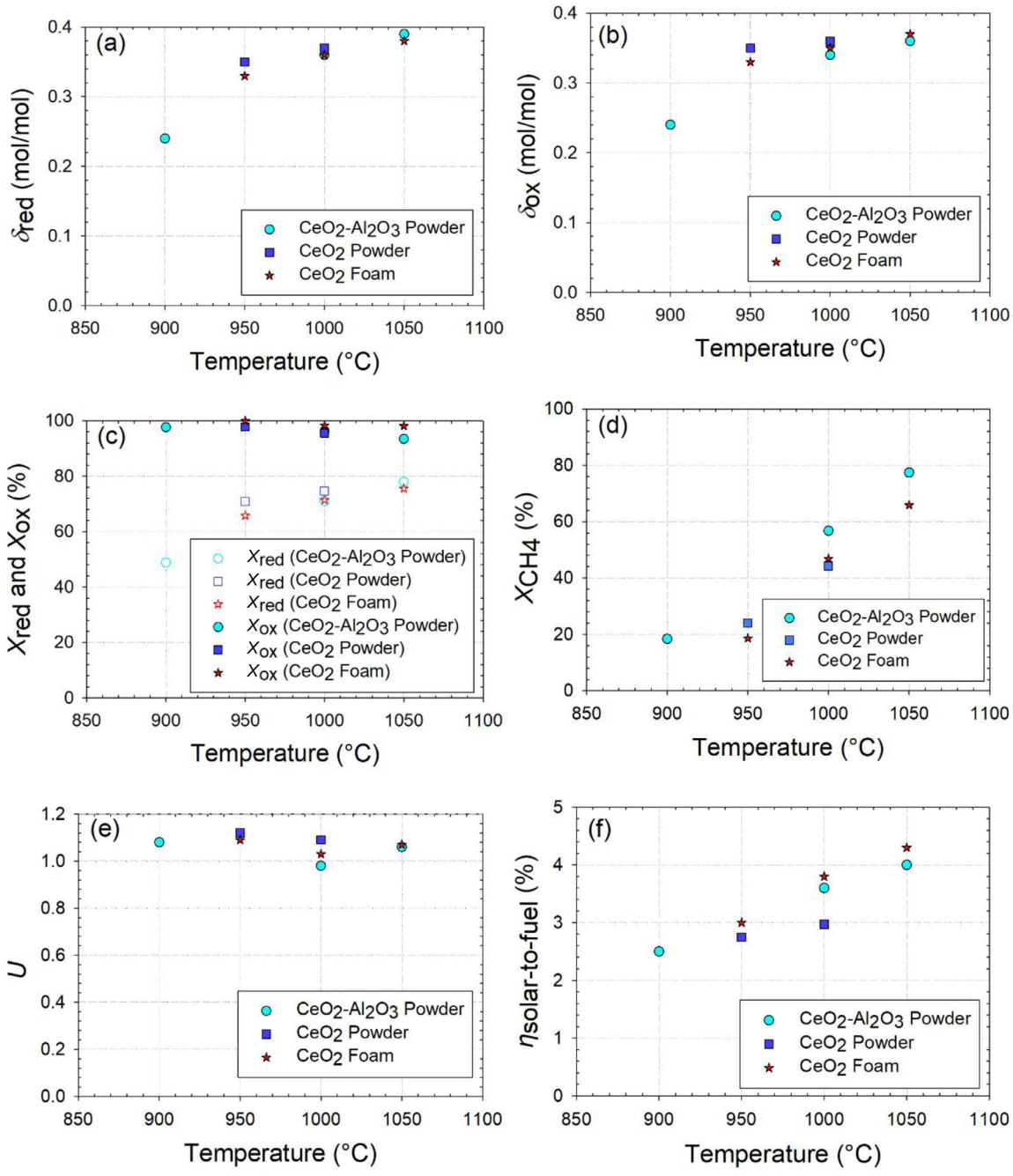

Fig. 8. Effect of temperature on (a) δ_{red}, (b) δ_{ox}, (c) reduction yield (X_{red}) and oxidation yield (X_{ox}), (d) CH_4 conversion (X_{CH_4}), (e) energy upgrade factor (U), and (f) solar-to-fuel energy conversion efficiency ($\eta_{solar\text{-}to\text{-}fuel}$) for different ceria structures.

oxidation with CO_2. This ceria was first reduced with a constant CH_4 flow-rate of 0.2 NL/min (50% CH_4 mole fraction at inlet) and subsequently re-oxidized with a constant CO_2 flow-rate of 0.2 NL/min (50% CO_2 mole fraction at inlet) at the same temperature.

Syngas production rates along with reactor temperature for both steps are presented in Fig. S10. During reduction step, the syngas production rates were higher at 1050 °C than at 1000 and 950 °C. For instance, the peak H_2 and CO production rates were 0.32 and 0.14 NL/min at 1050 °C compared to 0.21 and 0.10 NL/min at 950 °C. The reaction duration declined considerably with increasing temperature due to improved ceria reduction kinetics (from 24.4 min at 950 °C to 15.1 min at 1050 °C). During oxidation step, the peak CO production rate increased minimally from 0.14 to 0.16 NL/min while the oxidation duration decreased slightly (from 26 min at 950 °C to 22 min at 1050 °C). Therefore, the effect of temperature is not significant for the oxidation step with CO_2, which thus suggests low impact of kinetic reaction control for this step.

Fig. 9 shows the syngas yields quantified from the integration of the measured syngas production rates (Fig. S10) and reactor performance during reduction and oxidation steps. As expected, the CO (CeO_2+CH_4), H_2 (CeO_2+CH_4), H_2 (CH_4 cracking) yields, and δ_{red} increased with temperature, while the CO_2 (CeO_2+CH_4) yield remained the same (Fig. 9a). During oxidation step (Fig. 9b), an increase in the CO yield (2.89–3.12 mmol/g_{CeO_2}) was observed when increasing the temperature in the range of 950–1050 °C, thereby enhancing the δ_{ox} (0.37–0.40). The δ_{ox} values

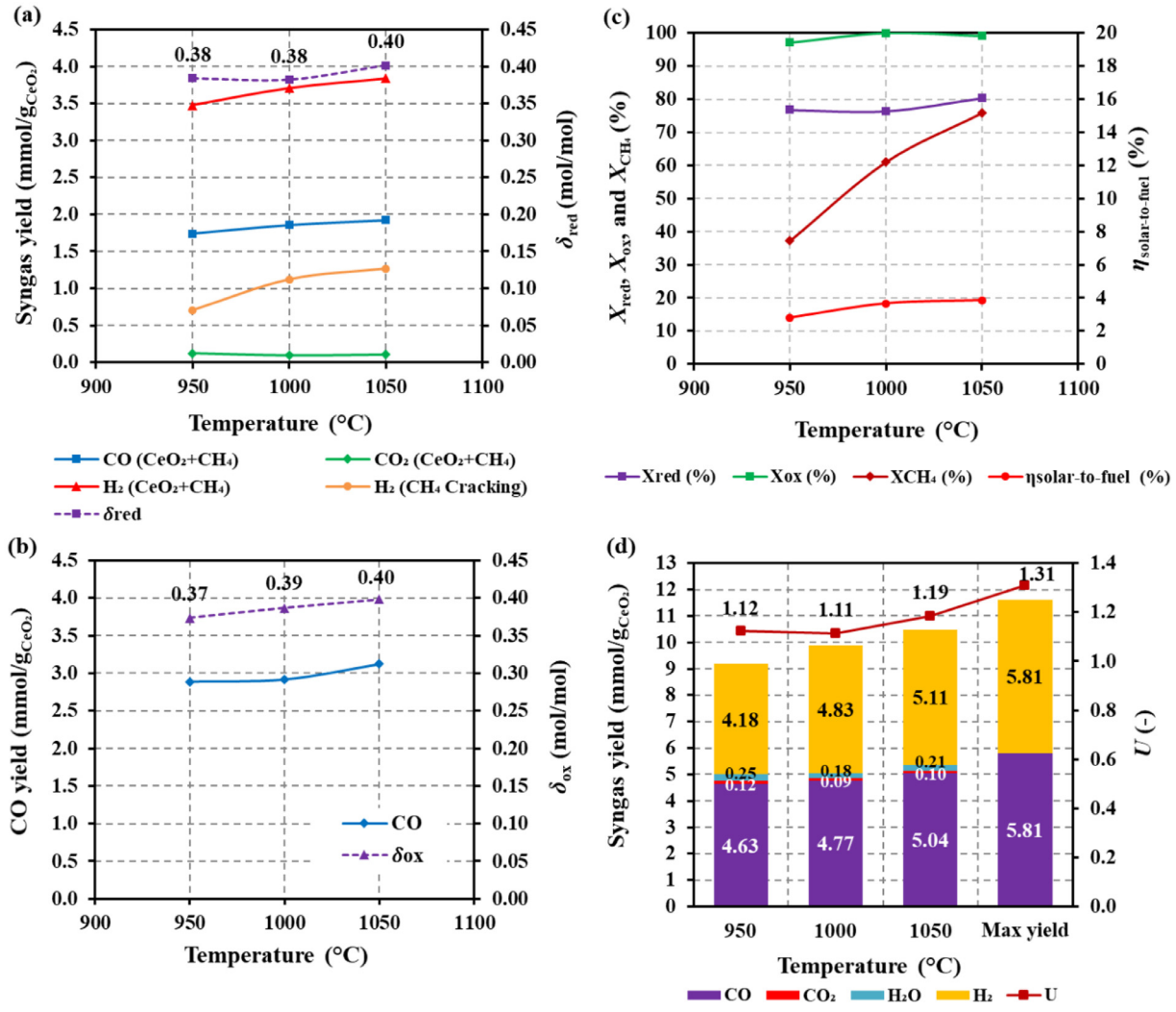

Fig. 9. Effect of temperature on (a) syngas yields and δ_{red} for reduction with CH_4, (b) CO yield and δ_{ox} for oxidation with CO_2 of CeO_2–Al_2O_3 blend cycled isothermally (CH_4 and CO_2 flow-rate of 0.2 NL/min), (c) ceria reduction/oxidation yields (X_{red}, X_{ox}), methane conversion (X_{CH_4}), and solar-to-fuel energy conversion efficiency ($\eta_{solar\text{-}to\text{-}fuel}$), and (d) energy upgrade factor (U) and total syngas yields obtained from both reduction and oxidation steps.

were similar to δ_{red}, thus confirming complete ceria re-oxidation with CO_2.

A temperature increase significantly enhanced the reactor performance (Fig. 9c), especially methane conversion (37.2%–75.8%). Fig. 9(d) compares the total syngas yield obtained from ceria cycles (sum of both steps) to the theoretical maximum yield (assuming that δ_{max}=0.5 in Eqs. (1) and (3), thereby yielding both 1 mol CO and 1 mol H_2 per mole CeO_2). Increasing temperature promoted the overall H_2 and CO yields with maximum measured values of 5.11 and 5.04 mmol/g_{CeO_2} at 1050 °C, respectively, while the maximum theoretical H_2 and CO yields that can be expected with CO_2 are 5.81 mmol/g_{CeO_2}. Note that the amounts of both H_2 and CO produced by side reactions (CH_4 cracking: $CH_4 \rightarrow C + 2H_2$ and carbon gasification: $C + CO_2 \rightarrow 2CO$) in both steps were taken into account in Fig. 9(d). The CO yield was close to the H_2 yield throughout the range. In addition, U was in the range 1.11–1.19 (vs. 1.31 for a stoichiometric reaction with δ_{max}=0.5).

3.5. Assessment of thermochemical stability during cycling

A pristine ceria reticulated foam (17.0152 g) sintered at 1000 °C for 6 h was used (Fig. S11a) to experimentally investigate the cycling stability during 6 consecutive cycles at 1000 °C (CH_4 flow rate of 0.2 NL/min for reduction step and H_2O flow-rate of 200 mg/min for oxidation step). N_2 was used as a carrier gas (2.2 NL/min).

Fig. 10 shows the syngas yields and reaction extents over six consecutive cycles during ceria reduction with methane (Fig. 10a) and ceria oxidation with H_2O (Fig. 10b). As expected, the H_2 (CeO_2+CH_4), CO, and CO_2 yields were constant over the whole cycling (ranging between 3.39 and 3.68 mmol/g_{CeO_2} for H_2, 1.69 and 1.84 mmol/g_{CeO_2} for CO, and 0.05 and 0.07 mmol/g_{CeO_2} for CO_2, Fig. 10a), thus validating ceria cycling stability. However, both small sintering and cracking lines within the sample were observed after the last cycle (Fig. S11b), presumably due to its weakened structure associated with low sintering temperature (1000 °C). Nevertheless, the redox cycling performance of ceria was not altered as reflected by a minimal fluctuation of reduction extent (δ_{red} in the range of 0.32–0.36). The H_2 (CH_4 cracking) yield fluctuated slightly (0.64–1.16 mmol/g_{CeO_2}), except for cycle 1 (2.00 mmol/g_{CeO_2}) in which the H_2 yield and δ_{red} were much higher due to a higher reduction temperature (1050°C) than the other cycles (the CO and CO_2 formed in the oxidation step were thus also higher, Fig. 10b).

Likewise, the H_2 ($CeO_{2-\delta}$+H_2O) yield produced by Eq. (2) (Fig. 10b) was fairly stable (1.94–2.05 mmol/g_{CeO_2}) thus leading to a similar stable δ_{ox} pattern (0.33–0.35). In addition, the quantities of $H_2(C + 2H_2O)$, $H_2(C + H_2O)$, $CO(C + H_2O)$, and $CO_2(C + 2H_2O)$

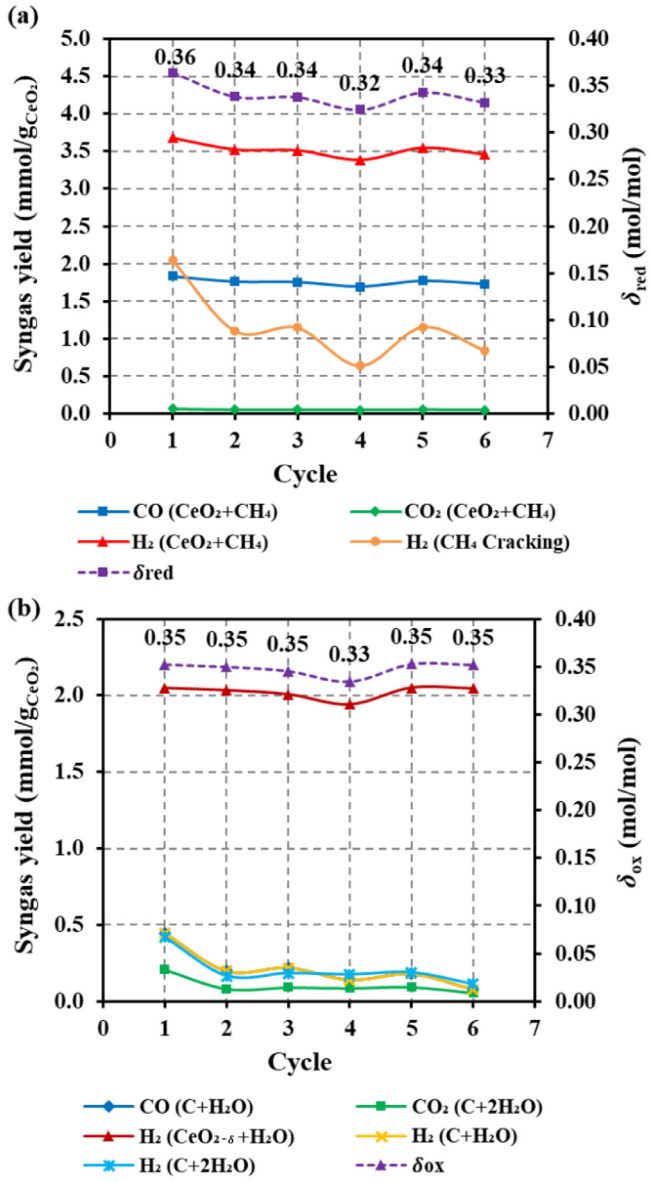

Fig. 10. Syngas yield and δ for both (a) reduction and (b) re-oxidation of ceria during 6 consecutive redox cycles performed at 1000 °C.

remained similar except for cycle 1 as mentioned above. Stable patterns in X_{red}, X_{ox}, X_{CH_4}, $\eta_{solar\text{-}to\text{-}fuel}$ and total syngas yield were consistently noticed (Fig. S12). Thus, the cycling stability of ceria can fairly be validated.

4. Conclusions

A solar process for methane reforming using solid oxidants has been developed, with final aim of producing syngas according to the following reaction: $CH_4 + M_xO_y \rightarrow M_xO_{y-1} + CO + 2H_2$. The key advantages of such a process with respect to the conventional process are: (i) generation of a gaseous mixture suitable for methanol synthesis, (ii) utilization of a solid oxidant instead of gaseous oxygen or steam water, (iii) absence of costly catalysts, and (iv) possible production of H_2 (or CO)-rich gas in a second step enabling the regeneration of the starting oxide. This chemical looping reforming process has been fully demonstrated using CeO_2 as the oxygen carrier material in the form of powders and reticulated porous foams within both fixed bed and volumetric solar reactor. Indeed, a directly irradiated 1.5 kW_{th} solar reactor has been successfully operated for solar-driven chemical looping methane reforming and isothermal H_2O/CO_2 splitting using different ceria structures as oxygen carriers, demonstrating the reliability and flexibility of the combined process towards syngas production. A parametric study was carried out focusing on the influence of sintering temperature of the foam structure, CH_4 flow-rate, operating temperature, type of oxidant (H_2O or CO_2), and ceria structures on averaged oxygen non-stoichiometry (δ), CH_4 conversion, syngas production, reactor performance, and thermochemical cycling stability:

- A high sintering temperature (1400 °C) adversely affects the syngas yield, methane conversion, and reactor performance, because of both lowered solid/gas interface area and lattice oxygen mobility, thus decreasing oxygen exchange capacity.
- Increasing the CH_4 flow-rate enhances δ (maximum value up to 0.41 for ceria powder), syngas production rate, and syngas yield. However, a remarkable decrease in CH_4 conversion is concomitantly observed (minimum value as low as 43% for CeO_2 powder). High CH_4 flow rate also favors CH_4 cracking reaction and carbon deposition, since the rate of methane decomposition exceeds the rate of ceria reduction. Such carbon deposition is not detrimental for the whole process since carbon is gasified in the oxidation step.
- Increasing the temperature (between 900 and 1050 °C) accelerates the rate of ceria reduction, which in turn significantly enhances the methane conversion (up to 77.4% for CeO_2–Al_2O_3 blend) and syngas yield and decreases the reduction step duration. However, it comes at the expense of favoring methane cracking, especially at 1050 °C. The $\eta_{solar\text{-}to\text{-}fuel}$ is increased with both CH_4 flow-rate and temperature (values in the range 1.14%–5.60%), while the energy upgrade factor up to 1.19 is accomplished with CO_2 as oxidant.
- The shape of ceria materials (packed-bed powder, foam) does not show any significant impact on both the syngas yield and δ but rather on CH_4 conversion and efficiency. The ceria foam shows better performance in terms of volumetric solar radiation absorption and uniform heating with lower solar power consumption compared to the other structures, thereby upgrading $\eta_{solar\text{-}to\text{-}fuel}$ (maximum value up to 5.6%). This implies that the foam structure is the most suitable to achieve high specific syngas production with reduced solar energy input.
- The ceria re-oxidation step is always complete (δ_{ox} and δ_{red} are similar), which means it is not kinetically limited, and it depends only on the extent of ceria reduction achieved during the previous reduction step. Ceria reduction (δ_{red}) is strongly dependent on temperature or methane flow rate, which thus denotes kinetically-controlled reaction rate.
- Stable patterns in the reduction/oxidation extents, syngas yields, and $\eta_{solar\text{-}to\text{-}fuel}$ during consecutive cycles for the ceria reticulated foam validate excellent thermal cycling stability.

The solar reactor concept is expected to be flexible in processing different ceria structures with varying particle sizes or geometries. Further work should be performed regarding reactor upscaling and ceria porous foam structure tailoring to improve the global efficiency of the integrated isothermal solar process combining chemical looping reforming and H_2O/CO_2 splitting.

Declarations of interest

None.

Acknowledgments

The King Mongkut's Institute of Technology Ladkrabang (KMITL), Thailand and the Franco-Thai scholarship program are gratefully acknowledged for fellowship granting.

Supplementary material

Supplementary material associated with this article can be found, in the online version, at doi:https://doi.org/10.1016/j.jechem.2019.05.004.

References

[1] A. Klerk, Kirk-Othmer Encyclopedia of Chemical Technology, Wiley, 2013.
[2] C. Graves, S.D. Ebbesen, M. Mogensen, K.S. Lackner, Renew. Sustain. Energy Rev. 15 (2011) 1–23.
[3] Q. Zheng, C. Janke, R. Farrauto, Appl. Catal. B Environ. 160–161 (2014) 525–533.
[4] Q. Song, R. Xiao, Y. Li, L. Shen, Ind. Eng. Chem. Res. 47 (2008) 4349–4357.
[5] G. Zhang, Y. Dong, M. Feng, Y. Zhang, W. Zhao, H. Cao, Chem. Eng. J. 156 (2010) 519–523.
[6] G. Zhang, A. Su, Y. Du, J. Qu, Y. Xu, J. Colloid Interface Sci. 433 (2014) 149–155.
[7] G. Zhang, Y. Du, Y. Xu, Y. Zhang, J. Ind. Eng. Chem. 20 (2014) 1677–1683.
[8] K. Otsuka, Y. Wang, M. Nakamura, Appl. Catal. A Gen. 183 (1999) 317–324.
[9] K. Otsuka, T. Ushiyama, I. Yamanaka, Chem. Lett. 22 (1993) 1517–1520.
[10] K. Otsuka, Y. Wang, E. Sunada, I. Yamanaka, J. Catal. 175 (1998) 152–160.
[11] C. Wieckert, A. Steinfeld, J. Sol. Energy Eng. 124 (2001) 55–62.
[12] T. Kodama, T. Shimizu, A. Aoki, Y. Kitayama, Energy Fuels 11 (1997) 1257–1263.
[13] H.I. Villafan-Vidales, S. Abanades, M. Montiel-Gonzalez, H. Romero-Paredes, Energy Technol. 5 (2016) 692–702.
[14] M. Welte, K. Warren, J.R. Scheffe, A. Steinfeld, Ind. Eng. Chem. Res. 56 (2017) 10300–10308.
[15] P. Furler, J. Scheffe, D. Marxer, M. Gorbar, A. Bonk, U. Vogt, Phys. Chem. Chem. Phys. 16 (2014) 10503–10511.
[16] D. Marxer, P. Furler, M. Takacs, A. Steinfeld, Energy Environ. Sci. 10 (2017) 1142–1149.
[17] S. Abanades, P. Charvin, G. Flamant, P. Neveu, Energy 31 (2006) 2805–2822.
[18] K. Otsuka, M. Hatano, A. Morikawa, J. Catal. 79 (1983) 493–496, doi:10.1016/0021-9517(83)90346-9.
[19] K. Li, H. Wang, Y. Wei, D. Yan, Appl. Catal. B Environ. 97 (2010) 361–372.
[20] K. Li, H. Wang, Y. Wei, D. Yan, Chem. Eng. J. 156 (2010) 512–518.
[21] T. Shimizu, Y. Kitayama, T. Kodama, Energy Fuels 15 (2001) 463–469.
[22] A. Steinfeld, A. Frei, P. Kuhn, D. Wuillemin, Int. J. Hydrog. Energy 20 (1995) 793–804, doi:10.1016/0360-3199(95)00016-7.
[23] M.M. Nair, S. Abanades, Energy Fuels 30 (2016) 6050–6058.
[24] O.T. Sørensen, J. Solid State Chem. 18 (1976) 217–233, doi:10.1016/0022-4596(76)90099-2.
[25] P.T. Krenzke, J.H. Davidson, Energy Fuels 28 (2014) 4088–4095.
[26] S. Chuayboon, S. Abanades, S. Rodat, Chem. Eng. J. 356 (2019) 756–770.
[27] P. Furler, J. Scheffe, M. Gorbar, L. Moes, U. Vogt, A. Steinfeld, Energy Fuels 26 (2012) 7051–7059.
[28] N. Siegel, R. Diver, J.E. Miller, T. Garino, S. Livers, Energy sustainability, in: Proceedings of the Third ASME International Conference on Energy Sustainability, 2, ASME, 2009, pp. 431–437.
[29] F.A. Costa Oliveira, M.A. Barreiros, S. Abanades, A.P.F. Caetano, R.M. Novais, R.C. Pullar, J. CO_2 Util. 26 (2018) 552–563.
[30] D. Arifin, A.W. Weimer, Sol. Energy 160 (2018) 178–185.
[31] M. Roeb, C. Sattler, R. Klüser, N. Monnerie, L. de Oliveira, A.G. Konstandopoulos, J. Sol. Energy Eng. 128 (2005) 125–133.
[32] T. Kodama, N. Gokon, Am. Chem. Soc. (2007) 4048–4077, doi:10.1021/cr050188a.
[33] P. Furler, J.R. Scheffe, A. Steinfeld, Energy Environ. Sci. 5 (2012) 6098–6103.
[34] L.J. Venstrom, N. Petkovich, S. Rudisill, A. Stein, J.H. Davidson, J. Sol. Energy Eng. 134 (2011) 11005–11008.
[35] T. Kodama, S. Bellan, N. Gokon, H. Seok Cho, Solar Energy 156 (2017) 113–132.
[36] E. Alonso, M. Romero, Renew. Sustain. Energy Rev. 41 (2015) 53–67.
[37] H.I. Villafán-Vidales, C.A. Arancibia-Bulnes, D. Riveros-Rosas, H. Romero-Paredes, C.A. Estrada, Renew. Sustain. Energy Rev. 75 (2017) 894–908.
[38] E. Koepf, I. Alxneit, C. Wieckert, A. Meier, Appl. Energy 188 (2017) 620–651.
[39] C. Agrafiotis, M. Roeb, C. Sattler, Renew. Sustain. Energy Rev. 42 (2015) 254–285.
[40] N. Piatkowski, C. Wieckert, A.W. Weimer, A. Steinfeld, Energy Environ. Sci. 4 (2011) 73–82.
[41] M. Puig-Arnavat, J.C. Tora, E.A Bruno, A. Coronas, Solar Energy 97 (2013) 67–84.
[42] K. Otsuka, E. Sunada, T. Ushiyama, I. Yamanaka, Stud. Surf. Sci. Catal. 107 (1997) 531–536.